Oden Institute REPORT 19-01

January 2019

Isogeometric Boundary Element Methods and Patch Tests for Linear Elastic Problems: Formulation, Numerical Integration, and Applications

by

Matthias Taus, Gregory J. Rodin, Thomas J. R. Hughes, and Michael A. Scott

Oden Institute for Computational Engineering and Sciences
The University of Texas at Austin
Austin, Texas 78712

Reference: Matthias Taus, Gregory J. Rodin, Thomas J. R. Hughes, and Michael A. Scott, "Isogeometric Boundary Element Methods and Patch Tests for Linear Elastic Problems: Formulation, Numerical Integration, and Applications," Oden Institute REPORT 19-01, Oden Institute for Computational Engineering and Sciences, The University of Texas at Austin, January 2019.

Isogeometric Boundary Element Methods and Patch Tests for Linear Elastic Problems: Formulation, Numerical Integration, and Applications

Matthias Taus[1], Gregory J. Rodin[2], Thomas J. R. Hughes[2], and Michael A. Scott[3]

[1] *Department of Mathematics, Massachusetts Institute of Technology, Cambridge, MA, 02139 USA*
[2] *Institute for Computational Engineering and Sciences, University of Texas at Austin, Austin, TX, 78712 USA*
[3] *Civil and Environmental Engineering, Brigham Young University, Provo, UT 84602 USA*

January 11, 2019

Abstract

An Isogeometric Boundary Element Method for solving three-dimensional boundary-value problems of classical linear elasticity theory is proposed. The method is developed as a generalization of author's earlier work on Laplace's equation to Navier's equations. As a result the proposed method features (*i*) proper basis functions for approximating Dirichlet and Neumann data, (*ii*) high-order collocation schemes for weakly singular, singular, and hyper-singular integral operators, (*iii*) state-of-the-art numerical integration schemes capable of handling geometries with disparate dimensions, (*iv*) well-conditioned linear algebraic systems, with the condition number independent of the mesh size. Boundary Element Patch Tests, as extensions of concepts widely used for finite element methods, are also introduced. It is shown how these tests can be used to assess the veracity of boundary element formulations and numerical integration schemes, implementations, and geometric precision of Computer Aided Design models. The method is applied to two challenging case studies, representative of industrial applications.

1 Introduction

This paper presents an Isogeometric Boundary Element Method (IgBEM) for solving three-dimensional boundary-value problems of classical elasticity theory. The term isogeometric means that both geometry and discretization are obtained directly from Computer Aided Design (CAD) tools, without any intermediate steps. Thus the proposed method allows one to circumvent major difficulties associated with volumetric mesh generation required by finite element methods, and consequently provides a direct pathway to a completely automated design-through-analysis pipeline.

IgBEMs have been previously considered in the context of both Collocation and Galerkin BEMs. Galerkin BEMs have a sound mathematical foundation and result in symmetric system matrices, but collocation BEMs are often preferred because they involve more efficient numerical integration schemes. This disadvantage of Galerkin methods becomes particularly significant for high-order isogeometric discretizations. This may partially explain why existing Galerkin IgBEMs are restricted to two-dimensional problems [1, 2, 3, 4, 5, 6, 7]. One notable exception is [8], where a three-dimensional Galerkin IgBEM for linear elastic problems is presented. Collocation IgBEMs have been applied to many different two- and three-dimensional problems, including to Laplace's equation [9, 10], linear elasticity [11, 12, 13, 14], acoustics [15, 16, 17], waves [18, 19], fracture mechanics [20], and shape-optimization [21, 22]. All of these IgBEMs are based on the singular integral equations, as collocation discretizations of the hyper-singular integral equations are not straightforward. This issue has been successfully addressed in [10], where collocation IgBEMs for Laplace's equation, involving both singular and hyper-singular integral equations, are developed. Those IgBEMs resulted in optimally converging and well conditioned methods. Collocation BEMs involving the hyper-singular integral equations can be beneficial for other classes of problems, such as acoustic scattering [15].

In this work, we introduce a collocation IgBEM that extends the results established in [10] to make the linear elastic hyper-singular integral equation accessible to collocation discretizations, introduce BEM patch tests, and demonstrate the applicability of our method to engineering problems involving complex geometries. We found patch tests to be a particularly useful development in the context of BEMs. We show that they can be used for the assessment of many different errors in BEMs including numerical schemes, computer implementations, and CAD models. A combination of all these aspects of patch tests allowed us to assess the accuracy of industrial problems involving complex geometries. We introduce all techniques in the context of IgBEMs but many of them, including patch tests, can be applied to other BEMs in exactly the same way.

1.1 Boundary element methods

Mathematical foundations for the proposed method have been developed in [10], where the focus was on isogeometric analysis of Boundary Integral Equations (BIEs) corresponding to boundary-value problems governed by Laplace's equation. In that paper, mathematical foundations available for BIEs defined on C^2-surfaces were exploited for developing numerical schemes for BIEs defined on $\tilde{C}^2$-surfaces, that is, surfaces that are C^2 almost everywhere, except for certain points and/or lines where the surfaces are only C^0. Such surfaces are ubiquitous to CAD models based on T-splines [23, 24, 25, 26, 27, 12] but not NURBS [28, 29]. While numerical schemes for BIEs defined on $\tilde{C}^2$-surfaces lack a rigorous mathematical foundation, numerical examples presented in [10] demonstrate that those schemes can attain optimal convergence rates established for BIEs defined on C^2-surfaces, and deliver very accurate numerical solutions. The numerical schemes developed in [10] include the following features:

- Proper basis functions for approximating Dirichlet and Neumann data.

- High-order collocation schemes for both singular and hyper-singular BIEs.
- All integral operators are evaluated as weakly-singular integrals, using state-of-the-art numerical integration schemes.
- BIEs are formulated in a way resulting in well-conditioned linear algebraic problems, with the condition number independent of the mesh size.

All of these features directly translate to BIEs corresponding to boundary-value problems for Navier's equations, except for the treatment of the adjoint double layer operator, whose evaluation requires a special representation. The aforementioned extensions from Laplace's to Navier's equations are straightforward because the smoothness of C^2-surfaces allows one to circumvent delicate issues ubiquitous to BIEs defined on less regular surfaces [30].

Since the emphasis of this paper is on applications rather than mathematical foundations, we paid particular attention to analysis of engineering structures with complex geometries which includes large aspect ratios and regions with relatively high curvature. For example, a turbine blade has disparate length, width, and thickness, and its leading edge may be sharp, so that its radius of curvature is very small. Upon discretization, BIEs for such geometries result in poorly conditioned linear algebraic systems [31], and therefore pose major difficulties for iterative solvers. Nevertheless, based on case studies considered in this paper, it appears that the accuracy of the proposed IgBEM is so good that problems of practical relevance require few enough degrees of freedom, so that one can use direct solvers, practically unaffected by poor conditioning. Geometries involving large aspect ratios and regions with relatively high curvature are also challenging for numerical integration schemes, even like the one implemented in [10], which incorporates state-of-the-art techniques for numerical treatment of weakly singular integrals. This is because the complex geometries involve near-singular maps between the parametric and physical spaces, and this aspect is simply not reflected even in state-of-the-art numerical integration schemes. We addressed this issue by augmenting the numerical integration scheme implemented in [10] with a hierarchical subdivision algorithm, which in effect regularizes near-singular geometric maps (see Appendix B).

1.2 The patch test

The patch test is a procedure used in finite element methods to assess the veracity of formulations and their computer implementations. The basic idea is that a properly formulated and implemented finite element method should be capable of exactly reproducing solutions to certain simple boundary-value problems up to round-off error. A typical use of the patch test in linear elasticity is based on displacement fields that are affine functions of spatial coordinates and therefore satisfy homogeneous Navier's equations exactly. The boundary conditions are set in accordance with the displacement fields and various element configurations are tested; the meshes can be uniform or non-uniform. The expectation for a properly formulated and implemented finite element method is that the computed solutions will be point-wise exact everywhere. This is what one may refer to as the engineering version of the patch test; see [32, Section 4.6, pp. 237-242], for a description and examples illustrating its

use. The engineering version of the patch test was devised by Bruce Irons, first described in [33], and later given a mathematical interpretation in the classic text of Strang and Fix [34, Section 4.5, pp. 174-181], in which it was extolled as "a simple but brilliant idea" and shown to be the key ingredient for mathematically assessing the convergence of non-conforming elements, an open problem theretofore. For further discussion of the engineering version of the patch test, see [35].

As far as we are aware, conceptions of the patch test appropriate for BEMs have never been given heretofore, and therefore we regard patch tests for BEMs as a primary contribution of the present paper. Like their finite element counterparts, BEM patch tests can be applied to numerical schemes and computer implementations, but they can be also used for assessing CAD models. Why have patch tests not been devised for BEMs? To answer this question, we need to examine properties of BEMs and their abilities to reproduce certain simple solutions exactly. We begin by noting that affine displacement fields, used in finite element patch tests, cannot be exactly reproduced with BEMs because BEMs involve singular integrals, for which no standard numerical integration scheme is exact on general surfaces. Consequently, the most we can hope for is to obtain exact solutions up to numerical integration errors. This places an onus on the integration schemes. Namely, upon refinement, their accuracy needs to be consistent with a mathematically predetermined convergence rate. We view this as a precondition for any viable BEM, and note that in our work we utilize an integration scheme that guarantee exponential convergence as the number of integration points per element in each parametric direction is increased [36]. This then becomes an essential feature of the BEM patch tests. Thus the issue of reproducing certain simple solutions exactly is a bit more involved than one might initially realize. In this context, we identify three BEM patch tests.

Interior Neumann Patch Test: This is the most broadly applicable patch test for BEMs corresponding to Neumann boundary-value problems defined on bounded domains. The boundary data for the Interior Neumann Patch Test are derived from a candidate affine displacement field, and in a successful Interior Neumann Patch Test the computed surface displacement field must be exact, up to integration error. We note that the traction field prescribed on the surface incorporates the unit normal field corresponding to the BEM surface discretization, and neither the discretization nor the unit normal field have to be exact, as long as the unit normal field is consistent with the surface, as dictated by equations of differential geometry. The Interior Neumann Patch Test is applicable to both isogeometric and conventional BEMs. It is particularly useful for identifying CAD models that are not watertight. Consequently, many NURBS-based models will not be able to pass the test, whereas watertight T-spline models will.

Interior Dirichlet Patch Test: In this case, the candidate affine displacement field generates the boundary data directly, and one solves for the surface traction field. The question that arises in this case is "Is the surface traction field exactly representable by the basis functions employed?" The answer to this question will be "yes" if the surface unit normal

field can be exactly spanned by the basis functions. Consequently, the Interior Dirichlet Patch Test will only be applicable to relatively simple geometries. For IgBEMs, these include polyhedra, spheres and tori; for conventional BEMs, with C^0 elements, only polyhedra would be candidate geometries.

Exterior Neumann Patch Test: Exterior problems are defined on infinite domains containing cavities. In these problems one specifies asymptotic conditions at infinity and boundary conditions on the cavity surface. BEMs are particularly effective for exterior problems because one needs to discretize the cavity surface only. For the Exterior Neumann Patch Test, we exploit the celebrated result of Eshelby [37] for ellipsoidal cavities which states that if the asymptotic conditions at infinity prescribe an affine displacement field and the cavity surface is traction-free, then the displacement field on the cavity surface is affine. Note that unlike the two interior patch tests, this one involves an affine displacement field only on the boundary but not in the entire domain. The Exterior Neumann Patch Test is restricted to IgBEMs because CAD basis functions are capable of representing all conic sections whereas conventional polynomial basis functions are not.

As a demonstration of the power of the proposed IgBEM and patch tests, we apply them to the analysis of two case studies representative of problems encountered in industrial applications within a fully automated design-through-analysis pipeline. Both cases involve T-spline CAD models analyzed elsewhere [12, 38], so that we can compare our predictions with those reported previously.

The remainder of the paper is organized as follows. In Section 2, we summarize the IgBEM and provide some implementation details. In Section 3, we focus on the patch tests. In Section 4, we present two case studies representative of industrial applications. In Section 5, we summarize key results and briefly discuss future work.

2 IgBEM

In this section, we summarize the governing BIEs and numerical schemes underlying the IgBEM defined on $\tilde{C}^2$ surfaces. Our presentation heavily relies on results developed in [10]. Also some of the details are presented in the appendices.

2.1 Model boundary-value problem

Consider a bounded domain $\Omega \subset \mathbb{R}^3$ with $\Gamma := \partial\Omega \in \tilde{C}^2$. The model boundary-value problem is formulated for Navier's equations of classical linear elasticity,

$$\mu u_{i,jj} + (\lambda + \mu) u_{j,ij} = 0 \quad \text{in } \Omega \,, \tag{1}$$

where u_i is the displacement field, and λ and μ are Lamé's constants. The boundary conditions include Dirichlet data, prescribed for the displacement vector

$$u_i = g_i \quad \text{on } \Gamma_D, \tag{2}$$

and Neumann data, prescribed for the traction vector

$$t_i := \mu(u_{i,j} + u_{j,i})n_j + \lambda u_{j,j} n_i = h_i \quad \text{on } \Gamma_N \,. \tag{3}$$

The surfaces Γ_D and Γ_N satisfy the usual restrictions $\overline{\Gamma_D \cup \Gamma_N} = \Gamma$ and $\Gamma_D \cap \Gamma_N = \emptyset$.

2.2 Integral equations

To define the governing BIEs one needs to introduce the fundamental solution

$$U_{ij}(x,y) = \frac{\lambda+\mu}{2\pi\mu(\lambda+2\mu)} \left[\frac{\lambda+3\mu}{\lambda+\mu} \frac{\delta_{ij}}{|x-y|} + \frac{(y_i - x_i)(y_j - x_j)}{|x-y|^3} \right] ,$$

and the Dirichlet-to-Neumann map γ_{ij}:

$$t_i(x) = \gamma_{ij}\left[u_j(x), x\right] := \left\{ n_k(x) \left[\mu \left(\delta_{ij}\delta_{kl} + \delta_{jk}\delta_{il} \right) + \lambda \delta_{ik}\delta_{jl} \right] \frac{\partial}{\partial x_l} \right\} u_j(x) \,,$$

where δ_{ij} is Kronecker's delta. Then the Singular BIE (SBIE) is expressed as

$$\left[\sigma_{ij}\mathcal{I} + \mathcal{K}_{ij}\right] u_j = \mathcal{V}_{ij} t_j \quad \text{on } \Gamma \,.$$

Similarly, the Hyper-Singular BIE (HSBIE) is expressed as

$$\left[(\delta_{ij} - \sigma_{ij})\mathcal{I} - \mathcal{K}'_{ij}\right] t_j = \mathcal{D}_{ij} u_j \quad \text{on } \Gamma \,.$$

In these equations, $\mathcal{I}$ is the identity operator,

$$\mathcal{V}_{ij} t_j(x) = \int_\Gamma U_{ij}(x,y) t_j(y) ds_y \quad x \in \Gamma$$

is the single-layer operator,

$$\mathcal{K}_{ij} u_j(x) = \int_\Gamma \gamma_{ik}\left[U_{kj}(x,y), y\right] u_j(y) ds_y \quad x \in \Gamma$$

is the double-layer operator,

$$\mathcal{K}'_{ij} t_j(x) = \int_\Gamma \gamma_{ik}\left[U_{kj}(x,y), x\right] t_j(y) ds_y \quad x \in \Gamma$$

is the adjoint double-layer operator,

$$\mathcal{D}_{ij} u_j(x) = -\int_\Gamma \gamma_{ik}\left\{\gamma_{kl}\left[U_{lj}(x,y), y\right], x\right\} u_j(y) ds_y \quad x \in \Gamma$$

is the hyper-singular operator, and

$$\sigma_{ij}(x) = -\int_\Gamma \gamma_{ik}\left[U_{kj}(x,y),y\right] ds_y \quad x \in \Gamma\,.$$

Note that for C^2-surfaces $\sigma_{ij} = \delta_{ij}/2$, but the adopted level of generality is necessary for $\tilde{C}^2$-surfaces.

Since the integral operators are defined via integrals over the entire Γ, one must extend both g_i and h_i onto the entire Γ. We denote the extensions by $\tilde{g}_i$ and $\tilde{h}_i$, and require $\tilde{g}_i$ to be $\tilde{C}^2(\Gamma)$, but allow $\tilde{h}_i$ to be discontinuous. Then the surface displacement and traction fields can be represented as

$$u_i = \tilde{u}_i + \tilde{g}_i \tag{4}$$

and

$$t_i = \tilde{t}_i + \tilde{h}_i\,, \tag{5}$$

with the obvious provisions $\tilde{u}_i|_{\overline{\Gamma_D}} = 0$ and $\tilde{t}_i|_{\overline{\Gamma_N}} = 0$. Accordingly, the SBIE and HSBIE are rewritten as

$$\mathcal{V}_{ij}\tilde{t}_j - \left[\sigma_{ij}\mathcal{I} + \mathcal{K}_{ij}\right]\tilde{u}_j = f_i^S \quad \text{on } \Gamma \tag{6}$$

and

$$\left[(\delta_{ij} - \sigma_{ij})\mathcal{I} - \mathcal{K}'_{ij}\right]\tilde{t}_j - \mathcal{D}_{ij}\tilde{u}_j = f_i^H \quad \text{on } \Gamma, \tag{7}$$

respectively, where

$$\begin{aligned} f_i^S &= \left[\sigma_{ij}\mathcal{I} + \mathcal{K}_{ij}\right]\tilde{g}_j - \mathcal{V}_{ij}\tilde{h}_j, \\ f_i^H &= \mathcal{D}_{ij}\tilde{g}_j - \left[(\delta_{ij} - \sigma_{ij})\mathcal{I} - \mathcal{K}'_{ij}\right]\tilde{h}_j. \end{aligned}$$

In this construction, the choice of extensions is not unique, but the recovered surface displacement and traction fields do not depend on how the extensions are chosen. Equations (6) and (7) are the governing BIEs for the IgBEM.

2.3 Discretization

Integral equations (6) and (7) are discretized using the approximations

$$\tilde{u}_i(x) \approx \tilde{u}_i^h(x) = \sum_{A=1}^{n^D} \underline{\tilde{u}}_i[A] N_A^D(x) \quad \text{and} \quad \tilde{t}_i(x) \approx \tilde{t}_i^h(x) = \sum_{A=1}^{n^N} \underline{\tilde{t}}_i[A] N_A^N(x), \tag{8}$$

where N_A^D and N_A^N are the basis functions, and $\underline{\tilde{u}}_i$ and $\underline{\tilde{t}}_i$ are column-vectors. The basis functions are such that $N_A^D(x) = 0$ for $x \in \Gamma_D$ and $N_A^N = 0$ for $x \in \Gamma_N$. The hyper-singular operator requires the basis functions N_A^D to be $\tilde{C}^2$. If the basis functions are T-splines

with $p = 3$, this requirement is automatically satisfied. In contrast, the basis functions N_A^N are acted upon by the single and adjoint double layer operators, and therefore can be discontinuous. To attain optimal approximations, N_A^N should have $p \geq 2$, and be C^1 almost everywhere, except for edges, corners, Neumann-Dirichlet interfaces, collapsed edges, and extraordinary points, where it must be discontinuous. This requirement follows directly from results which show that if the displacement field is approximated by T-splines of degree p and smoothness k, then the optimal approximation for the traction is of degree $p-1$ and smoothness $k-1$ [10]. However, we utilized T-splines with proper discontinuities but with $p = 3$ and $k = 2$ rather than $p = 2$ and $k = 1$. This choice of the basis functions did not prevent us from obtaining very accurate numerical solutions for boundary-value problems considered in this work.

Once the approximations for $\tilde{u}_i$ and $\tilde{t}_i$ have been introduced, the integral equations are discretized by collocating (6) at points x_A^D and (7) at points x_A^N. Those points can be defined as generalized Greville's abscissae; see [10, 12] for details. As a result one obtains the system of linear algebraic equations for $\underline{\tilde{u}}_i$ and $\underline{\tilde{t}}_i$:

$$V\underline{\tilde{t}} - \left(\Sigma^D + K\right)\underline{\tilde{u}} = \underline{f}^S \tag{9}$$

and

$$\left[\left(I^N - \Sigma^N\right) - K'\right]\underline{\tilde{t}} - D\underline{\tilde{u}} = \underline{f}^H. \tag{10}$$

These matrices can be assembled using the exact same techniques as in [10], only the adjoint double layer operator needs a new representation (see Appendix C). Detailed expressions for the matrices and column-vectors in these equations are given in Appendix A.

In this section, we heavily rely on similarities between fundamentals and numerical schemes for BIEs corresponding to Laplace's and Navier's equations, and therefore refer the reader to [10] for details. Nevertheless, there are two aspects in which these two classes of problems are different. First, from the mathematical perspective, the techniques for regularizing integral operators are somewhat different, although the end result is the same: all integral operators can be evaluated using weakly-singular integrals; see Appendix C for details. Second, from the engineering perspective, many components designed for structural applications include rounds, fillets, thin walls, and other features associated with disparate lengths. For these types of problems, we developed a numerical integration scheme in which elements with large aspect ratios and/or curvatures are hierarchically partitioned, so that numerical integration errors are tightly controlled; see Appendix B for details.

3 Patch Tests

3.1 Formulation

For simplicity of presentation, we develop BEM patch tests by considering linear rather than affine displacement fields in the form

$$u_i(x) = \alpha_{ij} x_j \,, \tag{11}$$

where α_{ij} is a constant symmetric second rank tensor. These fields satisfy Navier's equations, and their rigid body motion consists of zero translation and rotation with respect to the origin. For Dirichlet boundary-value problems, (11) also defines prescribed boundary data and implies uniqueness. For Neumann boundary-value problems, the boundary data is derived from (11),

$$t_i(x) = \lambda\alpha_{kk}n_i(x) + 2\mu\alpha_{ij}n_j(x)\,, \tag{12}$$

and uniqueness is achieved by nullifying the rigid body motion with respect to the origin.

For $x \in \Gamma$,

$$x_j = \varphi_j(s) = \sum_A P_{A,j}\tilde{N}_A(s), \tag{13}$$

where s denotes parametric coordinates, the $P_{A,j}$'s are the coordinates of the control points in isogeometric analysis or nodes in conventional BEMs, and $\tilde{N}_A$ are the basis functions in the parametric domain, i.e. $\tilde{N}_A = N_A \circ \varphi$. The discretized displacement field is written as

$$u_i^h\left[\varphi(s)\right] = \sum_A u_{A,i}\tilde{N}_A^D(s),$$

where the $u_{A,i}$'s are the control point, or nodal, values of the discrete displacement field. The isoparametric hypothesis [32] amounts to using the same basis functions for approximation and geometry, i.e. $\tilde{N}_A^D = \tilde{N}_A$. If we select $u_{A,i} = \alpha_{ij}P_{A,j}$, then

$$u_i^h\left[\varphi(s)\right] = \sum_A \alpha_{ij}P_{A,j}\tilde{N}_A^D(s) = \alpha_{ij}\sum_A P_{A,j}\tilde{N}_A(s) = \alpha_{ij}x_j = u_i(x),$$

which demonstrates that the discrete displacement field is also capable of representing the exact linear displacement field.

The discretized traction field is written as

$$t_i^h\left[\varphi(s)\right] = \sum_A t_{A,i}\tilde{N}_A^N(s),$$

where the $t_{A,i}$'s are the control point, or nodal, values of the discrete traction field, and $\tilde{N}_A^N$ are the basis functions in the parametric domain If the unit normal field can be exactly represented by the traction basis functions, i.e.

$$n_i\left[\varphi(s)\right] = \sum_A n_{A,i}\tilde{N}_A^N(s),$$

and we set

$$t_{A,i} = n_{A,i}\lambda\alpha_{kk} + 2\mu\alpha_{ij}n_{A,j},$$

then

$$
\begin{aligned}
t_i^h\left[\varphi(s)\right] &= \sum_A \left[n_{A,i}\lambda\alpha_{kk} + \mu\alpha_{ij}n_{A,j}\right]\tilde{N}_A^N(s) \\
&= \lambda\alpha_{kk}\sum_A n_{A,i}\tilde{N}_A^N(s) + \mu\alpha_{ij}\sum_A n_{A,j}\tilde{N}_A^N(s) \\
&= \lambda\alpha_{kk}n_i(x) + \mu\alpha_{ij}n_j(x) = t_i(x).
\end{aligned}
$$

This demonstrates that the discrete traction field is capable of representing the exact traction field, only when the unit normal field can be exactly represented by the traction basis functions $\tilde{N}_A^N$. In the context of isogeometric analysis, we are aware of only three classes of geometries for which NURBS or T-splines can exactly represent the unit normal field: polyhedra, spheres, and tori. In these cases, reliance on the isoparametric hypothesis for approximating the traction field becomes irrelevant.

Now it is appropriate to ask the question "In what sense can the candidate fields be exactly represented by either isogeometric or conventional BEM basis functions?" To answer this question, we observe that the BIE kernels involve singular kernels, for which no standard numerical integration scheme is exact on general surfaces. One notable exception is the exact evaluation of singular integrals on polyhedrons (or polyhedral meshes); for details see [39] and references therein. In this paper, with the emphasis on CAD geometries, we ignore this exception, and adopt the notion that the accuracy of computed displacement fields is dominated by numerical integration. From this perspective, in a successful BEM patch test, the error must decay as the number of integration points per element in each parametric direction is increased, and the rate of decay must be mathematically predetermined. We view this requirement as a precondition for any viable BEM, and therefore the essential feature of a BEM patch test. In our work we utilize rules that guarantee exponential convergence of numerical integration errors as the number of integration points per element in each parametric direction is increased [36]. If the error converges to zero exponentially and only stagnates at a level similar to machine precision, we consider the patch test to be passed. If the error stagnates at a level well above machine precision, or does not converge exponentially, it implies that there are additional sources of error, and the patch test is failed. In certain situations, those additional sources of error can be identified which we show in turn. We will see that this information can be used to assess new formulations, numerical schemes, and their implementations. Once their validity has been established, patch tests can be used to assess the quality of CAD models and/or the error due to integration schemes (see Section 4). Both are important, as CAD representations with gaps are ubiquitous, and numerical integration often controls the accuracy of BEM computations.

The difference in approximations for the displacement and traction fields give rise to two distinct patch tests.

Interior Neumann Patch Test: For this test, we prescribe Neumann boundary data defined in (12) and solve the SBIE (9) for $u_i^h(x)$. This approximation should always be exact,

for any geometry, as long as the surface geometry is watertight. Consequently, this may be viewed as a *universal* patch test applicable to both isogeometric and conventional BEMs.

Interior Dirichlet Patch Test: For this test, we prescribe Dirichlet data defined in (11) and solve the HSBIE (10) for $t_i^h(x)$. We expect to compute the exact traction field only if the unit normal field can be exactly spanned by the basis functions of the traction field. This condition holds for polyhedra for all discretizations, for spheres and tori in isogeometric discretizations, but not for more general geometries, even simple ones such as general ellipsoids.

Exterior Neumann Patch Test: There is a class of exterior problems, discovered by Eshelby [37], in which the linear displacement fields are realized only on the boundary rather then the entire domain. A boundary-value problem of interest is formulated for an ellipsoidal traction-free cavity and asymptotic conditions $u_i(x) = \alpha_{ij}x_j$ as $|x| \to \infty$. For this problem, one can establish that the governing BIE is

$$\left[\frac{1}{2}\mathcal{I} - \mathcal{K}_{ij}\right] u_j = \alpha_{ij}x_j \quad \text{on } \Gamma\,, \tag{14}$$

and the solution $u_i(x)$ of this integral equation is a linear field on Γ; this field can be constructed following [37]. This approximation should be exact for watertight ellipsoids. Since ellipsoidal surfaces can be exactly represented by cubic NURBS or T-splines, this patch test is applicable to IgBEMs but not conventional BEMs. However, highly oblate or prolate ellipsoids may pose significant challenges for numerical integration because maps from the physical to parametric space are near-singular, and therefore one needs a robust scheme capable of handling such maps; see Appendix B.

3.2 Numerical examples

In this section, we illustrate the use of the patch tests on a suite of interior and exterior boundary-value problems. For all patch tests, correctly posed according to the aforementioned requirements, the only source of error should be due to numerical integration. In the numerical integration scheme utilized herein this error will decay to zero (up to round-off error) exponentially fast, as the number of integration points per (Bézier) element is increased in each parametric direction. This would amount to patch tests being passed. If the error stagnates, or decays at a slower rate, there are sources of error other than numerical integration, or there is an error in the integration scheme. In what follows, we presume that the integration scheme is correct.

In all examples, we set $\lambda = \mu = 1$ and

$$\alpha_{ij} = \begin{pmatrix} -1/4 & 0 & 0 \\ 0 & -1/4 & 0 \\ 0 & 0 & 1 \end{pmatrix}$$

This choice corresponds to a uniaxial stress $\sigma_{33} = 5/2$. Numerical experiments with other choices of the elastic constants and α_{ij} resulted in very similar quantitative and qualitative results. The error was defined as the L_2-norm of the difference between the numerical and exact solutions normalized by the L_2-norm of the exact solution. The norm was defined with respect to the boundary data of interest.

3.2.1 Interior Neumann Patch Test for general geometries

To confirm that the Interior Neumann Patch Test is passed by any geometry we consider three geometries: a unit sphere, a prolate spheroid, and a regularly perturbed unit sphere, generated by the parametrization

$$\begin{aligned} x &= (1 + \varepsilon \sin 8\phi_1)\,(1 + \varepsilon \sin 16\phi_2) \cos\phi_1 \sin\phi_2 \\ y &= (1 + \varepsilon \sin 8\phi_1) \sin\phi_1 \sin\phi_2 \\ z &= (1 + \varepsilon \sin 16\phi_2) \cos\phi_1 \end{aligned}$$

where $\varepsilon = 0.1$, $\phi_1 \in [-\pi/2, \pi/2]$, and $\phi_2 \in [0, 2\pi]$ (see Figure 1). All geometries were constructed using Grasshopper$^{\text{TM}}$ and Rhinoceros$^{\text{TM}}$. The plots for the error versus the

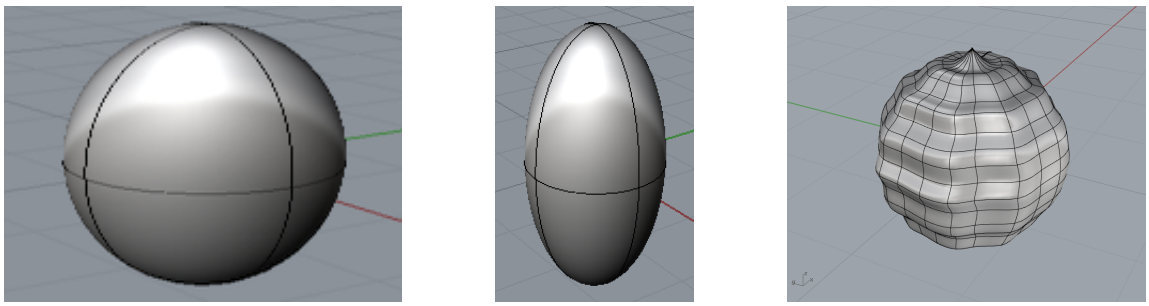

Figure 1: Parametrization of the sphere (left), the prolate spheroid (center), and the perturbed sphere (right).

number of integration points per element in each parametric direction are shown in Figure 2. As expected, all errors exhibit exponential decay which indicates that the Interior Neumann Patch Test is passed for all three geometries. This confirms that the Interior Neumann Patch Test has to be passed on any watertight geometry as long as the SBIE is correctly implemented.

3.2.2 Interior Neumann Patch Test for non-watertight geometries

To demonstrate that the Interior Neumann Patch Test can be used to detect non-watertight geometries, let us consider two unit cubes generated by six quadratic NURBS patches with no continuity enforced over patch boundaries. The first cube is perfect with no gaps. The second cube is imperfect, and to describe the imperfection let us introduce a coordinate system such that $0 \leq x_1 \leq 1$, $0 \leq x_2 \leq 1$, and $0 \leq x_3 \leq 1$. Note that since no continuity is enforced over patch boundaries, there are 9 control points per patch, and since the control points are not shared by the patches the total number of control points is 54. Then there are

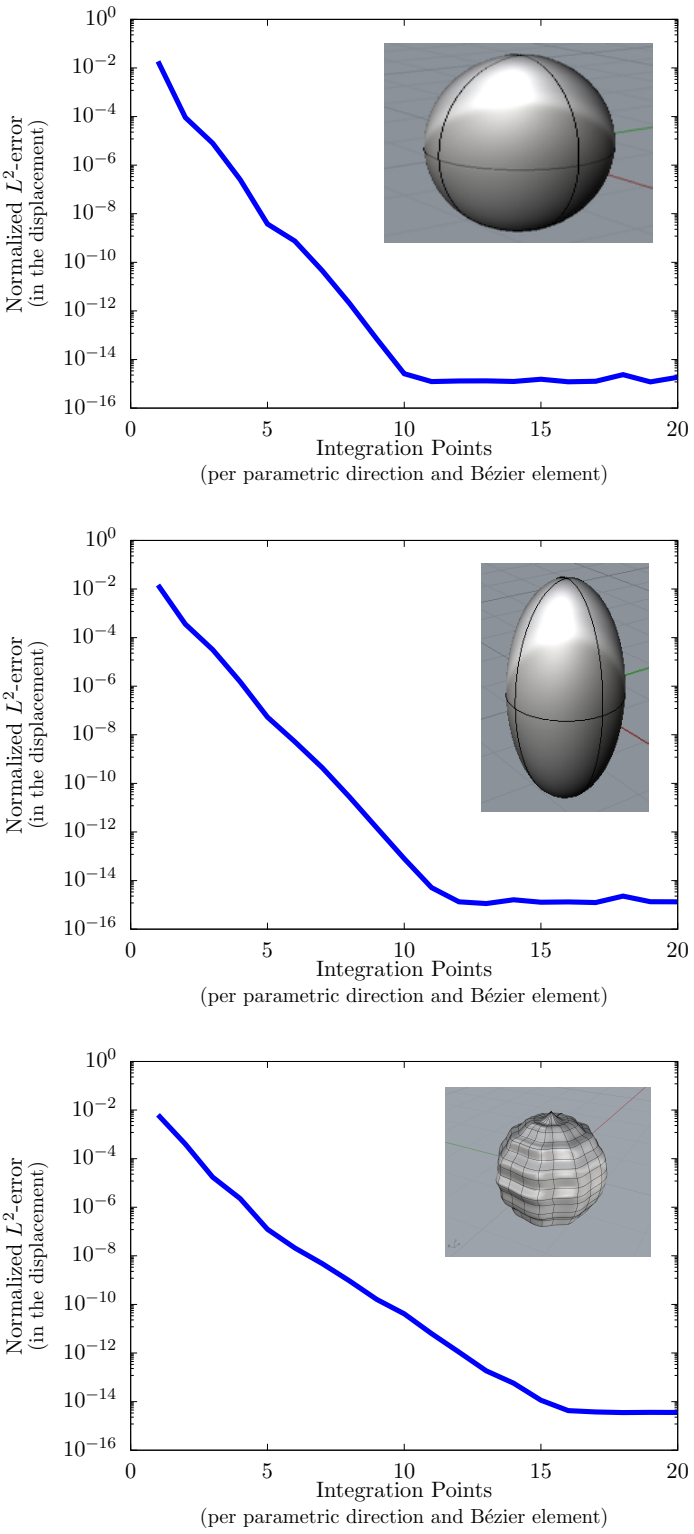

Figure 2: Interior Neumann Patch Tests: The error versus the number of integration points per element in each parametric direction for the normalized L^2-error of the displacement field for the unit sphere (top), the prolate spheroid (center), and the perturbed sphere (bottom).

three control points at each corner. To create an imperfection we displace the control point at the corner (1,1,0) corresponding to the patch in the plane $x_1 = 1$ by 10^{-3} along positive x_1. This results in bending of the patch and opens two gaps, between the bent patch and the patches in the planes $x_2 = 1$ and $x_3 = 0$. Results for the Interior Neumann Patch Test are shown in Figure 3. For the perfect cube, the error decays exponentially as the number of integration points per element in each parametric direction is increased, whereas for the imperfect cube the error stagnates indicating that the surface is not closed. The magnitude of the stagnated error is $\mathcal{O}(10^{-4})$, which is only one order of magnitude less than the gap size. While there is no simple explanation why the error is not closer to the gap size, it is also clear that the error could be used as a rough estimate for the gap size. This technique may be used to assess the magnitude of errors produced by imperfections in the geometry, e.g. gaps or overlaps, which are common in trimmed NURBS models.

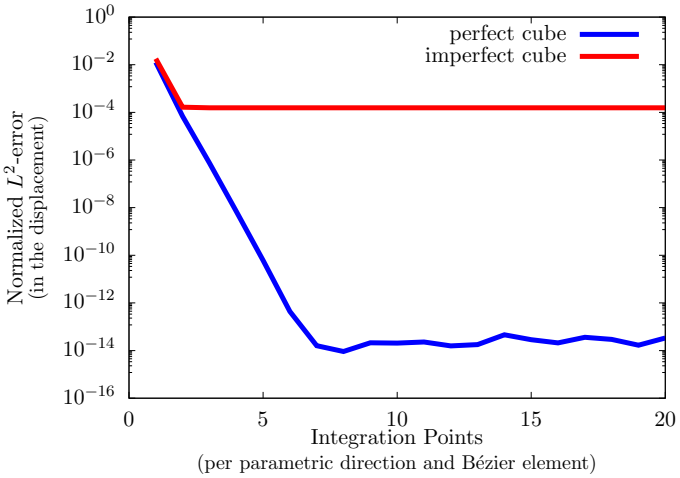

Figure 3: Interior Neumann Patch Tests: The error versus the number of integration points per element in each parametric direction for the perfect and imperfect cube.

In addition, the gaps can be located by plotting the local error of the displacement field. Figure 4 shows the error of the displacement field for the imperfect cube, and clearly indicates that there are problems near the corner (1,1,0).

3.2.3 Interior Dirichlet Patch Test for a sphere and spheroid

Now we confirm that the Interior Dirichlet Patch Test is only passed by geometries whose unit normal field can be spanned exactly by cubic T-splines used to approximate the traction field. To this end, we consider three geometries: the same sphere and spheroid as in Section 3.2.1, and the perfect cube from Section 3.2.2. It is clear that the unit normal field of the cube is constant on each face and discontinuous over the edges. Therefore, the traction field is piecewise constant and can be exactly represented by the T-splines used for approximation. Consequently, we expect that the cube would pass the test. The unit sphere ($\kappa = 1$) and

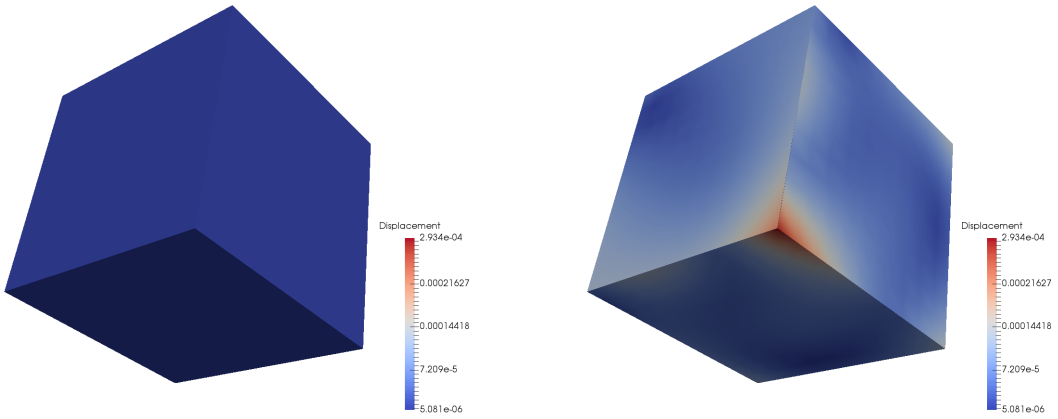

Figure 4: The plot of the local error for the perfect (top) and imperfect (bottom) cube.

the prolate spheroid ($\kappa = 2$) can be defined by the equation

$$x_1^2 + x_2^2 + \left(\frac{x_3}{\kappa}\right)^2 = 1.$$

Then the unit normal fields for the sphere and spheroid are

$$n(x) = \begin{pmatrix} x_1 \\ x_2 \\ x_3 \end{pmatrix} \quad \text{and} \quad n(x) = \frac{1}{\sqrt{x_1^2 + x_2^2 + x_3^2/\kappa^4}} \begin{pmatrix} x_1 \\ x_2 \\ x_3/\kappa^2 \end{pmatrix},$$

respectively. Thus for the sphere the unit normal field is a linear field, and it can be exactly spanned by cubic T-splines. This is not the case for the prolate spheroid. Consequently, we expect that the sphere would pass the test but the spheroid would not.

The plots for the error versus the number of integration points per element in each parametric direction are shown in Figure 5. As expected, the data for the sphere and cube exhibit exponential decay, whereas the data for the prolate spheroid stagnates at a value corresponding to the approximation error for the unit normal field. The results for the sphere and cube indicate the Interior Dirichlet Patch Test is passed. The results for the spheroid indicate that the Interior Dirichlet Patch Test is failed. This confirms that for a correctly implemented HSBIE using a suitable integration rule, the Interior Dirichlet Patch Test is only passed for geometries whose unit normal field can be represented by the basis functions used to approximate the traction field.

3.2.4 Exterior Neumann Patch Test for exact ellipsoids

To confirm that the Exterior Neumann Patch Test is passed by any ellipsoid, we consider spheroids with aspect ratios $\kappa = 0.01, 0.1, 0.5, 1, 2, 10, 100$; $\kappa < 1$ ($\kappa > 1$) represents oblate (prolate) spheroids. Each of the spheroids is (exactly) parametrized by T-splines using 8 elements. The plots for the error versus the number of integration points per element in

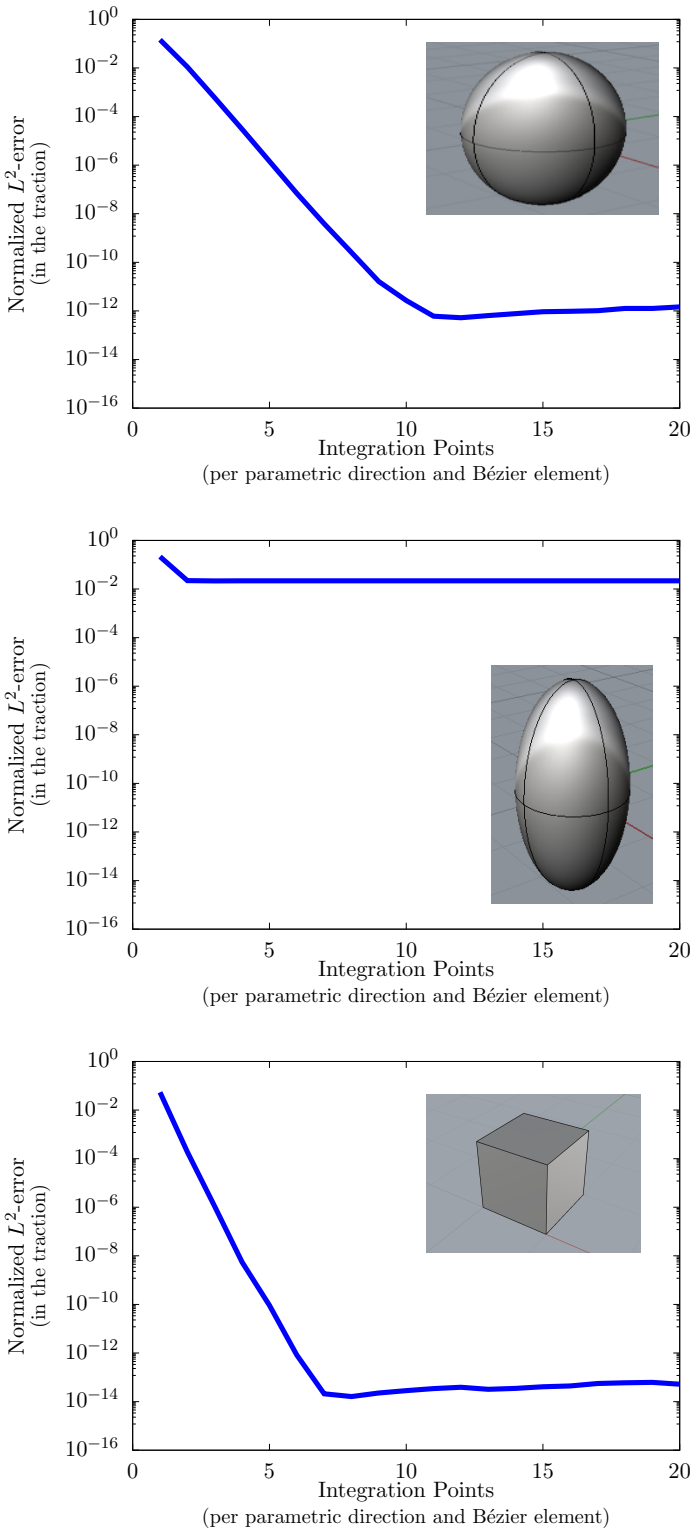

Figure 5: Interior Dirichlet Patch Tests: The error versus the number of integration points per element in each parametric direction for the normalized L^2-error of the traction field for the unit sphere (top), the prolate spheroid (center), and the cube (bottom).

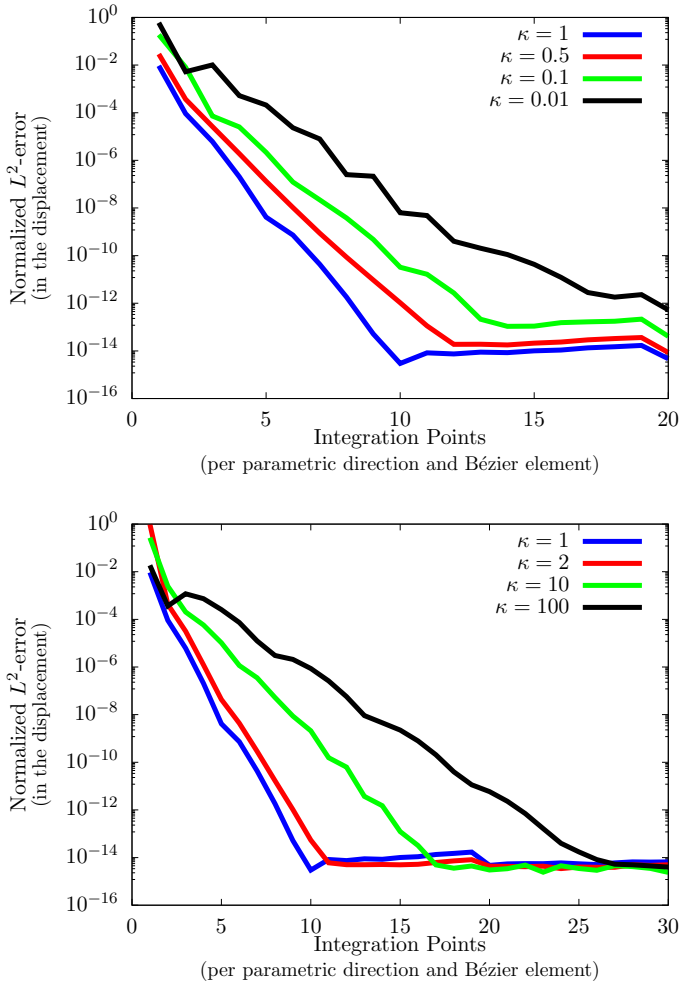

Figure 6: Exterior Neumann Patch Tests: The error versus the number of integration points per element in each parametric direction for the normalized L^2-error of the displacement field for spheroids with different aspect ratios κ (top: oblate spheroids, bottom: prolate spheroids).

each parametric direction are shown in Figure 6. It is clear that for all geometries the errors converge exponentially to machine precision.

To show that the construction of a suitable integration rule for spheroids with high aspect ratios is not trivial, let us consider the same test but without the additional subdivision scheme described in Appendix B. The plots for the error versus the number of integration points per element in each parametric direction are shown in Figure 7. It is clear that the

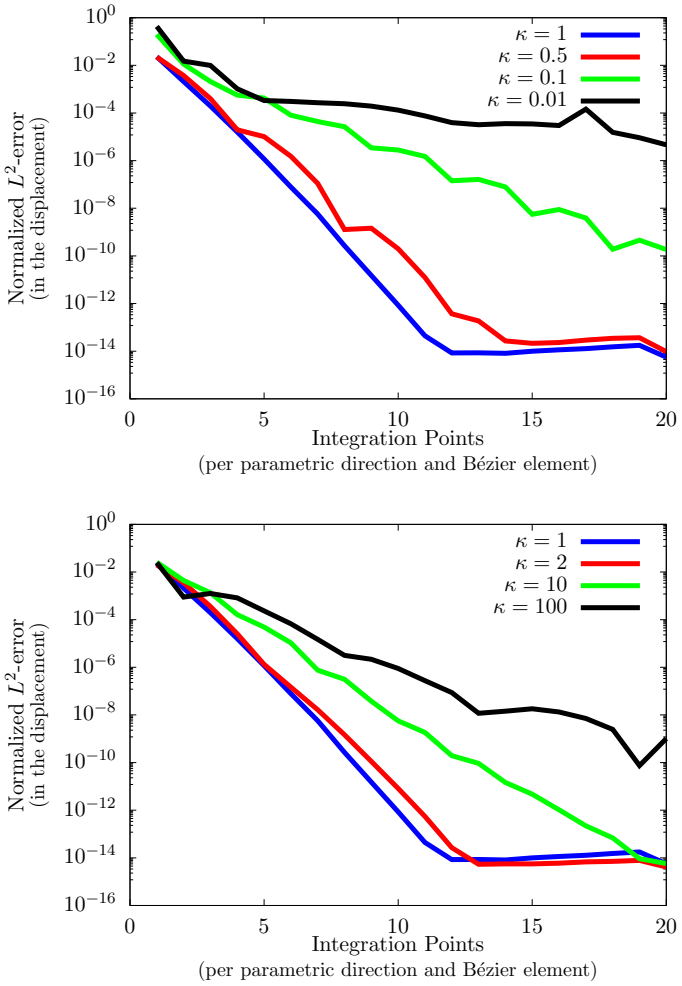

Figure 7: Exterior Neumann Patch Tests: The error versus the number of integration points per element in each parametric direction for the normalized L^2-error of the displacement field for spheroids with different aspect ratios κ (top: oblate spheroids, bottom: prolate spheroids), without an additional subdivision scheme to account for high curvature and aspect ratios.

errors converge exponentially to zero for all cases. However, it is also clear that the error reduction is rather slow for either $\kappa \ll 1$ or $\kappa \gg 1$. This is because such spheroids involve regions of high curvature. Further, prolate spheroids with $\kappa \gg 1$ involve Bézier elements

with very high aspect ratios. Both geometric features significantly affect the numerical integration scheme and in principle can result in unacceptable errors. This demonstrates how the Exterior Neumann Patch Test can be used for evaluating and designing numerical integration schemes.

4 Case Studies

In this section, we present computational results for two case studies representative of industrial applications. Both cases involve T-spline CAD models and have been analyzed previously using a different IgBEM [12] and an immersed isogeometric finite element method [38]. In this paper, each case is analyzed in two stages: (i) the T-spline CAD model is assessed with an Interior Neumann Patch Test, and (ii) the boundary-value problem corresponding to boundary conditions specified in the original paper is solved.

4.1 A propeller subjected to a wind load

4.1.1 Geometry and patch tests

The first case involved an aluminum propeller (Young's modulus $E = 100GPa$ and Poisson's ratio $\nu = 0.3$) subjected to a wind load. Following [12] and [38], the propeller was specified using a CAD file generated using Rhinoceros$^{\text{TM}}$ and T-Splines$^{\text{TM}}$. This CAD representation involved 5,136 Bézier elements and 48 extraordinary points (Figs. 8 and 9).

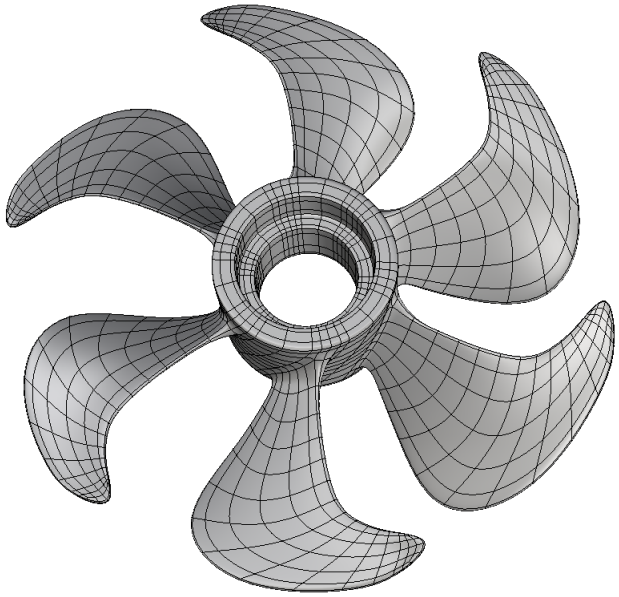

Figure 8: The CAD geometry of the propeller.

The CAD model was first subjected to an Interior Neumann Patch Test using the prescribed

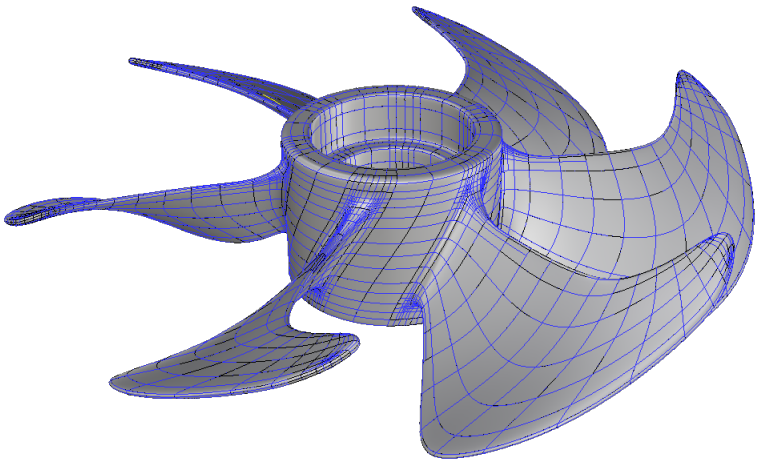

Figure 9: The Bézier element mesh of the propeller.

traction field

$$t_i = \sigma_{ij} n_j = -\delta_{i3} n_3 \, ;$$

the rigid body translation and rotation were set equal to zero at the origin. Results of this test are presented in Figure 10, where the normalized L^2-error of the surface displacement field is plotted versus the number of integration points per element in each parametric direction. This plot clearly shows that, as the number of integration points per element in each parametric direction is increased, (i) the error is reduced exponentially, and (ii) the error can be reduced to 10^{-9}. We accepted this as a confirmation that the CAD model was sufficiently watertight.

Once we had established that the geometry was suitable, we switched to the automated integration scheme, in which the number of integration points per element in each parametric directions is determined using simple local rules; see Appendix B for details. The automated integration rule is designed so that it does not adversely affect the convergence rate of the approximation error, and this condition is realized using a minimal number of integration points per element in each parametric direction. Therefore, the error introduced by the automated integration scheme was treated as a lower bound for the error expected for the solution of the main problem. If this error was unacceptable, the mesh inherited from the CAD geometry would have to be refined. For our problem, we determined that the L^2-error for the surface displacement field was $\mathcal{O}\left(10^{-3}\right)$. We regarded this error as acceptable, and proceeded to the main problem.

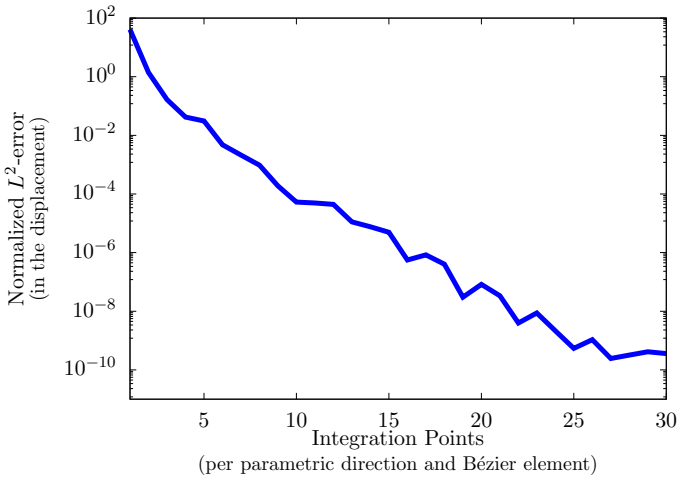

Figure 10: Interior Neumann test: The error versus the number of integration points per element in each parametric direction for the propeller.

4.1.2 Main problem

The wind load was simulated by assigning zero displacement field on the interior cylindrical surface of the hub, as shown in Figure 11, while the remaining boundary was subjected to the traction field as

$$t = [0, 0, -Pn_3 H(n_3)] \ ,$$

where $P = 1\,kPa$ is the wind pressure, H is the Heavyside function, and x_3 is the symmetry axis of the propeller pointing upward. The boundary-value problem specified here is exactly the same as specified in [12]. In the original paper, E and P were specified using inconsistent units, and we took this into account while comparing our results with the original ones.

Figure 12 shows the deformed shape of the propeller, where the displacement field is exaggerated by a factor of 1000. The deformed geometry is colored using the magnitude of the displacement field, and shown in relation to the Bézier mesh of the original geometry. The lack of smoothness of the Bézier mesh is due to post-processing only. Figure 13 shows the von Mises stress. Note that both fields exhibit the expected six-fold symmetry.

It is somewhat difficult to compare our results with those in [12]. For the displacement field, the original paper provides only the deformed shape but no information for quantifying the displacement field. For the von Mises stress, the original results are somewhat similar to ours. However, there are significant differences. In particular, our analysis identifies high-stress regions only near the hub, whereas in the original analysis there are also high-stress regions at the blade tips. High-stress regions near the hub are straightforward to explain using elementary beam theory, by assuming that each blade is a cantilever beam subjected to a uniformly distributed load. With this assumption, we estimated the maximum von Mises stress to be $5.7MPa$, which compares favorably with the computational results. We

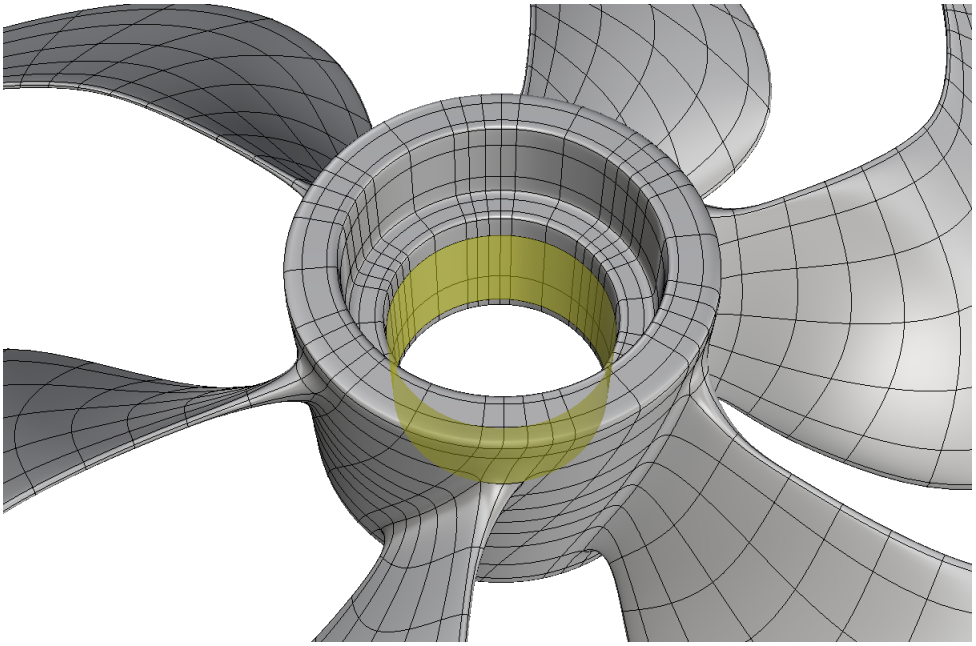

Figure 11: The Dirichlet boundary, highlighted in yellow, for the wind loading on the propeller.

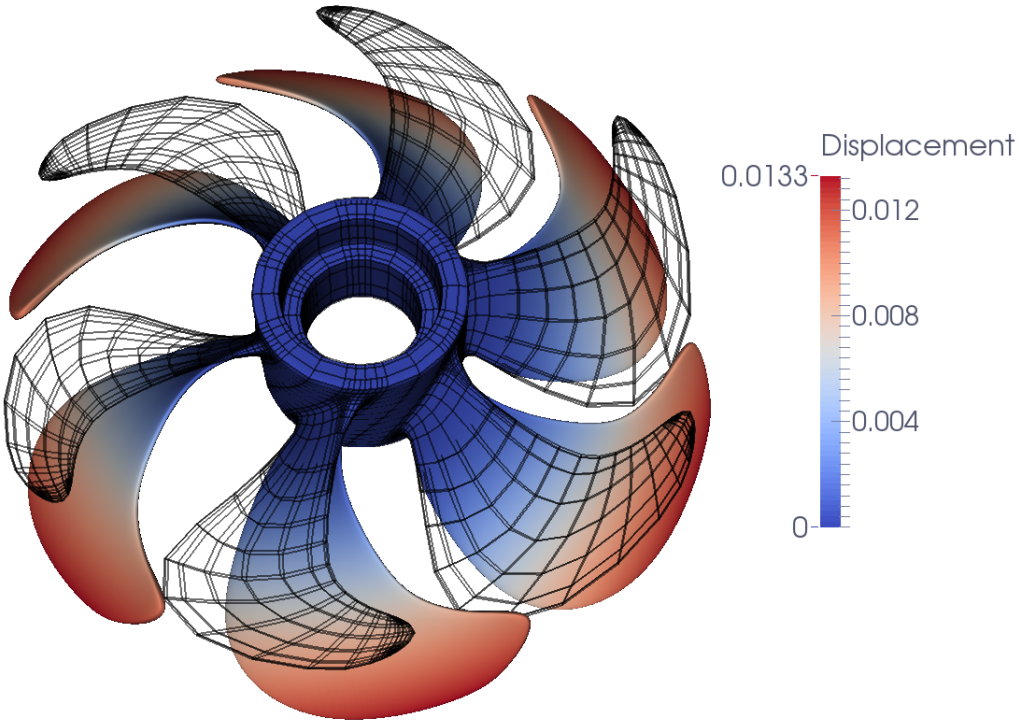

Figure 12: The deformed geometry exaggerated by a factor of 1000. The propeller is colored by the magnitude of the displacement field and shown in relation to the Bézier mesh of the original geometry.

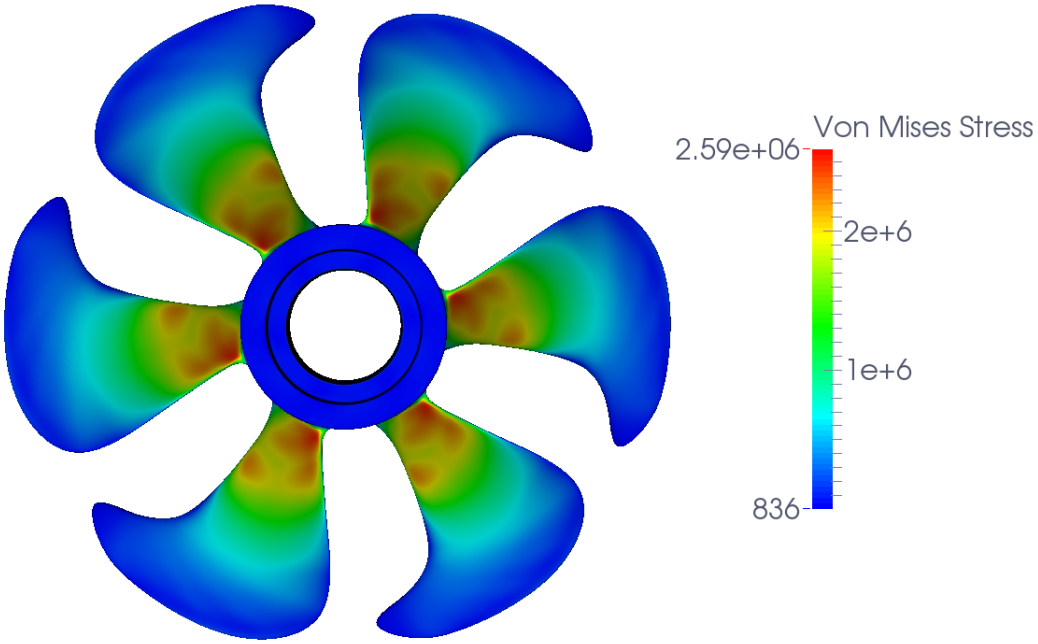

Figure 13: The von Mises stress.

believe that the difference between the two sets of computational results is primarily due to significantly different integrations schemes. In the original paper, no special provisions were made for the near-singular integration, whereas in the integration scheme of this paper the near-singular integration is a focal point.

4.2 The rim of a car wheel

4.2.1 Geometry and patch tests

The second problem involves an aluminum rim of a car wheel (Young's modulus $E = 70GPa$ and Poisson's ratio $\nu = 0.34$) subjected to a load mimicking contact. The rim radius $R = 239mm$, height $h = 223mm$, measured along the y-axis, and the wall thickness $w = 5mm$ (Fig. 14). The rim was specified using a CAD file generated using Rhinoceros$^{\text{TM}}$ and T-Splines$^{\text{TM}}$. The CAD representation involved 11,712 Bézier elements and 96 extraordinary points (Figs. 15 and 16).

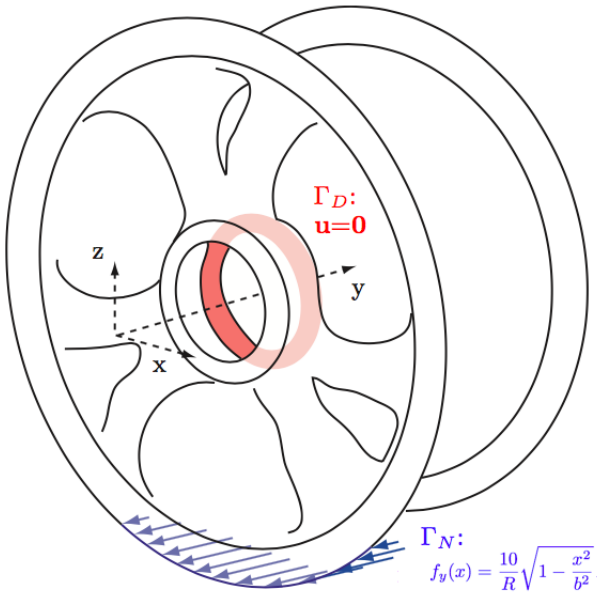

Figure 14: A schematic view of the rim.

For this geometry we did not test the CAD model for watertightness but we did subject the CAD model to the Interior Neumann Patch Test with the fixed automated integration scheme in order to get a lower bound for the error we can expect for the main problem. We determined that the normalized L^2-error for the surface displacements is $\mathcal{O}(10^{-5})$. We regarded this error as acceptable and proceeded to the main problem.

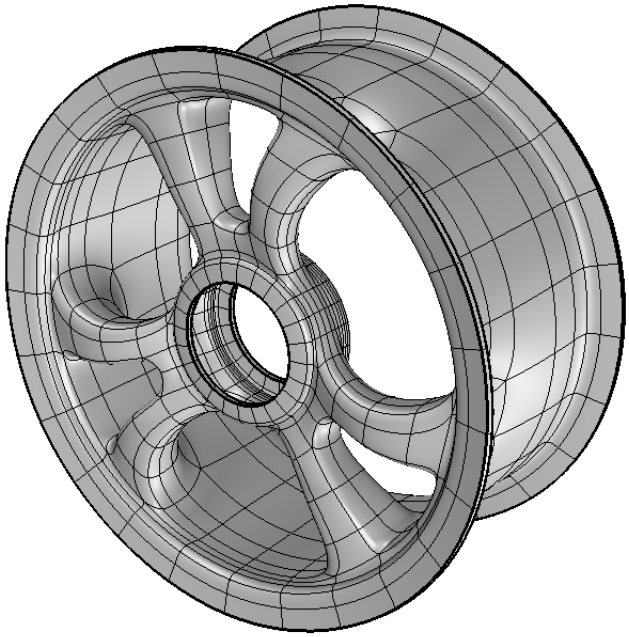

Figure 15: The CAD geometry of the rim.

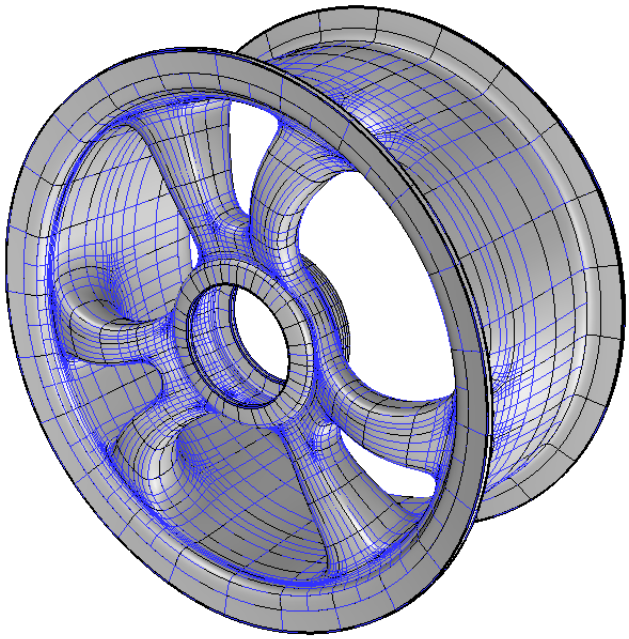

Figure 16: The Bézier element mesh of the rim.

4.2.2 Main problem

We simulated lateral forces induced by the car turning by assigning zero displacement field on the hub of the rim (see Figure 17), and the traction field (see Fig. 17)

$$t = \left[0, \frac{F}{Rw}\sqrt{1 - \frac{x^2}{b^2}}, 0\right]$$

where $F = 10kN$ and $b = R\sin(\pi/5)$. The rest of the boundary is set to be traction-free. The boundary conditions are summarized in Figure 14.

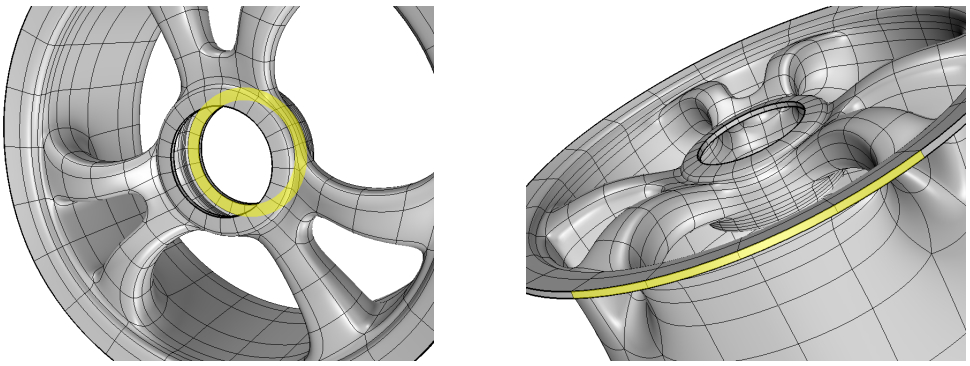

Figure 17: The Dirichlet (left) and non-zero Neumann (right) boundaries highlighted in yellow.

To accommodate the prescribed boundary conditions, we had to change the original CAD file because our implementation of the IgBEM only allows for prescribing boundary conditions on an element-by-element basis, and the prescribed traction field is not aligned with the elements in the original CAD file. To this end, we had to subdivide two elements in the original T-spline model into two sub-elements. This is a straightforward change since T-splines naturally allow for hanging nodes.

Figure 18 shows the deformed shape of the rim, where the displacement field is exaggerated by a factor of 300. The deformed geometry is colored using the magnitude of the displacement field. Figure 19 shows the von Mises stress. Figures 18 and 19 should be compared to Figures 50 and 51 in [38], respectively. For comparison purposes, we rescaled the color map of the von Mises stress to the same ones as in [38]. For the displacement field, our results are similar to the ones computed in [38]: the maximum displacement in [38] is $0.64mm$, and ours is $0.59mm$. While the von Mises stress maps also look similar, our prediction for the maximum stress is much larger than that in the original paper. This can be explained as follows. The original paper relies on an immersed finite element method, which does not exploit the T-splines of the geometric model as the basis functions. The advantage of this approach is that it allows for mesh refinement without changing the geometric model. However, as it is the case for all immersed finite element methods, the basis functions do not conform with the geometric model, and therefore are not ideal for computing surface and near-surface data. This challenge for immersed methods is currently being researched.

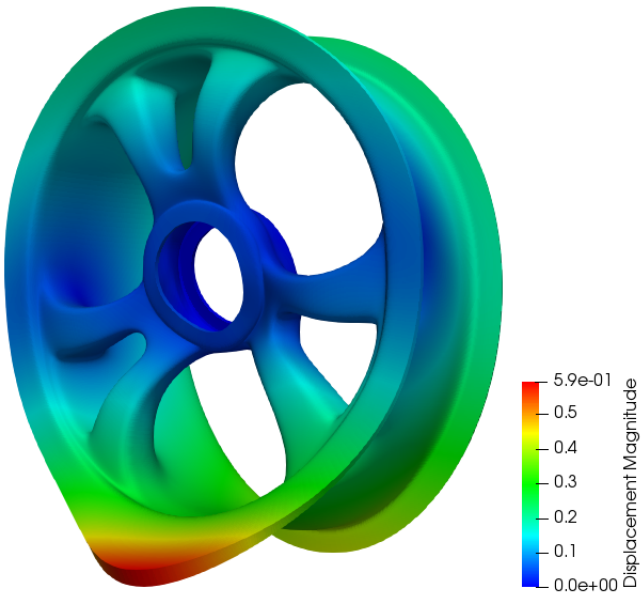

Figure 18: The deformed shape exaggerated by a factor of 300. The rim is colored by the magnitude of the displacement field.

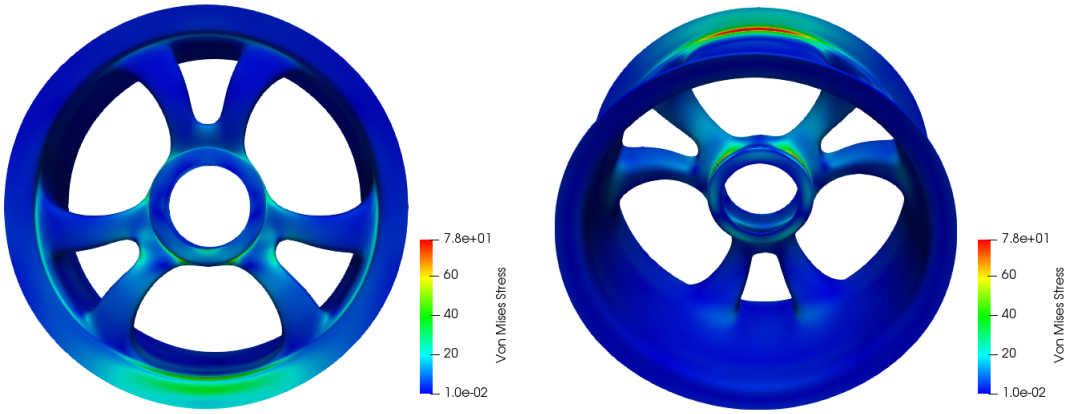

Figure 19: The Von Mises Stress on the rim.

5 Concluding Remarks

In this paper we have presented an Isogeometric Boundary Element Method for linear elasticity problems that generalizes the method we developed previously for Laplace's equation [10]. Particular attention was paid to the development of numerical integration schemes applicable to domains with fine-scale features, regions of high curvature, large aspect ratios, rounds, and fillets; see Appendix B for details.

A focus of this paper has been the development of BEM patch tests, an extension of the well-known finite element patch test concept, which has proved invaluable in the development of finite element methods. The utility of patch tests is multifold. They can be used to assess the veracity of a formulation, locate flaws in a discrete model (e.g., gaps and overlaps between patches in CAD models), expose coding errors, identify shortcomings of a numerical integration procedure, etc. We proposed and described three different patch tests, the Internal Neumann and Dirichlet Patch Tests, and the External Neumann Patch Test. Each of these tests queries different aspects of a formulation, providing independent information to assess the validity of a method and its implementation. The Internal Neumann Patch Test is applicable to isogeometric and conventional BEMs. However, the other two patch tests are geometrically restrictive and it seems only isogeometric discretizations have the geometric precision to employ them.

In our work we have employed direct solvers, but the research thrust in BEMs has been iterative solvers [40, 41, 42, 43]. Significant progress has been made for many problem classes, but structural analysis problems provide unique challenges. Engineering structures are often very thin, have large aspect ratios, possess regions of very high curvature, feature sharp edges, etc. The propeller example is representative. It would be an enormously valuable contribution to develop an efficient and robust iterative solver for this class of problems.

In this paper we used the first commercialization of T-splines, the industrial design plugin T-Splines$^{\text{TM}}$ for the NURBS modeler Rhinoceros$^{\text{TM}}$. The success of this tool led to the acquisition of T-Splines$^{\text{TM}}$ by Autodesk$^{\text{TM}}$ and the integration of T-splines into several major CAD packages, including Fusion 360$^{\text{TM}}$. However, while T-splines have been successfully applied in the context of isogeometric analysis, their commercial support is still mainly focused on design rather than analysis.

Recently proposed U-splines [44] are intended to subsume and improve T-splines, by adding robustness and flexibility to both design and analysis. We believe that those improvements will significantly impact the proposed IgBEM, and result in an implementation with full commercial support.

6 Acknowledgement

T.J.R. Hughes was supported by grants from the Office of Naval Research (N00014-08-1-0992), the National Science Foundation (CMMI-01101007), and SINTEF (UTA10-000374) with the University of Texas at Austin. G. J. Rodin was supported by a grant from the National Science Foundation (CMMI 1663551), MTS fellowship at the University of Minnesota, and Moncrief Grand Challenge Faculty Award from Institute for Computational Engineering and Sciences at the University of Texas at Austin. M. Taus was partially supported by a Fulbright fellowship, a NIMS graduate fellowships, and the National Science Foundation (CMMI-01101007). We are grateful to Prof. Dominik Schillinger of University of Minnesota for his help with analyzing the rim problem.

References

[1] A. Aimi, M. Diligenti, M. L. Sampoli, and A. Sestini, "Isogemetric analysis and symmetric Galerkin BEM: A 2D numerical study," *Applied Mathematics and Computation*, vol. 272, pp. 173–186, 2016.

[2] A. Aimi, M. Diligenti, M. L. Sampoli, and A. Sestini, "Non-polynomial spline alternatives in Isogeometric Symmetric Galerkin BEM," *Applied Numerical Mathematics*, vol. 116, pp. 10–23, 2017.

[3] B. H. Nguyen, H. D. Tran, C. Anitescu, X. Zhuang, and T. Rabczuk, "An isogeometric symmetric Galerkin boundary element method for two-dimensional crack problems," *Computer Methods in Applied Mechanics and Engineering*, vol. 306, pp. 252–275, 2016.

[4] A. Aimi, F. Calabrò, M. Diligenti, M. Sampoli, G. Sangalli, and A. Sestini, "Efficient assembly based on B-spline tailored quadrature rules for the IgA-SGBEM," *Computer Methods in Applied Mechanics and Engineering*, vol. 331, pp. 327–342, 2018.

[5] M. Feischl, G. Gantner, and D. Praetorius, "Reliable and efficient a posteriori error estimation for adaptive IGA boundary element methods for weakly-singular integral equations," *Computer Methods in Applied Mechanics and Engineering*, vol. 290, pp. 362–386, 2015.

[6] M. Feischl, G. Gantner, A. Haberl, and D. Praetorius, "Adaptive 2D IGA boundary element methods," *Engineering Analysis with Boundary Elements*, vol. 62, pp. 141–153, 2016.

[7] M. Feischl, G. Gantner, A. Haberl, and D. Praetorius, "Optimal convergence for adaptive IGA boundary element methods for weakly-singular integral equations," *Numerische Mathematik*, vol. 136, no. 1, pp. 147–182, 2017.

[8] B. H. Nguyen, X. Zhuang, P. Wriggers, T. Rabczuk, M. E. Mear, and H. D. Tran, "Isogeometric symmetric Galerkin boundary element method for three-dimensional elasticity problems," *Computer Methods in Applied Mechanics and Engineering*, vol. 323, pp. 132–150, 2017.

[9] J. Gu, J. Zhang, and G. Li, "Isogeometric analysis in BIE for 3-D potential problem," *Engineering Analysis with Boundary Elements*, vol. 36, no. 5, pp. 858–865, 2012.

[10] M. Taus, G. J. Rodin, and T. J. R. Hughes, "Isogeometric analysis of boundary integral equations: High-order collocation methods for the singular and hyper-singular equations," *Mathematical Models and Methods in Applied Sciences*, vol. 26, no. 08, pp. 1447–1480, 2016.

[11] R. N. Simpson, S. P. A. Bordas, J. Trevelyan, and T. Rabczuk, "A two-dimensional Isogeometric Boundary Element Method for elastostatic analysis," *Computer Methods in Applied Mechanics and Engineering*, vol. 209-212, pp. 87–100, 2012.

[12] M. A. Scott, R. N. Simpson, J. A. Evans, S. Lipton, S. P. A. Bordas, T. J. R. Hughes, and T. W. Sederberg, "Isogeometric boundary element analysis using unstructured T-splines," *Computer Methods in Applied Mechanics and Engineering*, vol. 254, pp. 197 – 221, 2013.

[13] Y. Wang, D. J. Benson, and A. P. Nagy, "A multi-patch nonsingular isogeometric boundary element method using trimmed elements," *Computational Mechanics*, vol. 56, no. 1, pp. 173–191, 2015.

[14] G. Beer, B. Marussig, and J. Zechner, "A simple approach to the numerical simulation with trimmed CAD surfaces," *Computer Methods in Applied Mechanics and Engineering*, vol. 285, pp. 776–790, 2015.

[15] R. N. Simpson, M. A. Scott, M. Taus, D. C. Thomas, and H. Lian, "Acoustic isogeometric boundary element analysis," *Computer Methods in Applied Mechanics and Engineering*, vol. 269, pp. 265–290, 2014.

[16] M. J. Peake, J. Trevelyan, and G. Coates, "Extended isogeometric boundary element method (XIBEM) for three-dimensional medium-wave acoustic scattering problems," *Computer Methods in Applied Mechanics and Engineering*, vol. 284, pp. 762–780, 2015. Isogeometric Analysis Special Issue.

[17] L. Coox, O. Atak, D. Vandepitte, and W. Desmet, "An isogeometric indirect boundary element method for solving acoustic problems in open-boundary domains," *Computer Methods in Applied Mechanics and Engineering*, vol. 316, pp. 186–208, 2017. Special Issue on Isogeometric Analysis: Progress and Challenges.

[18] K. A. Belibassakis, T. P. Gerostathis, K. V. Kostas, C. G. Politis, P. D. Kaklis, A. I. Ginnis, and C. Feurer, "A BEM-isogeometric method for the ship wave-resistance problem," *Ocean Engineering*, vol. 60, pp. 53–67, 2013.

[19] A. I. Ginnis, K. V. Kostas, C. G. Politis, P. D. Kaklis, K. A. Belibassakis, T. P. Gerostathis, M. A. Scott, and T. J. R. Hughes, "Isogeometric boundary-element analysis for the wave-resistance problem using T-splines," *Computer Methods in Applied Mechanics and Engineering*, vol. 279, pp. 425–439, 2014.

[20] X. Peng, E. Atroshchenko, P. Kerfriden, and S. P. A. Bordas, "Isogeometric boundary element methods for three dimensional static fracture and fatigue crack growth," *Computer Methods in Applied Mechanics and Engineering*, vol. 316, pp. 151–185, 2017.

[21] K. Li and X. Qian, "Isogeometric analysis and shape optimization via boundary integral," *Computer-Aided Design*, vol. 43, no. 11, pp. 1427–1437, 2011. Solid and Physical Modeling 2011.

[22] S. H. Sun, T. T. Yu, T. T. Nguyen, E. Atroshchenko, and T. Q. Bui, "Structural shape optimization by IGABEM and particle swarm optimization algorithm," *Engineering Analysis with Boundary Elements*, vol. 88, pp. 26–40, 2018.

[23] T. W. Sederberg, J. Zheng, A. Bakenov, and A. Nasri, "T-splines and T-NURCCs," *ACM Transaction on Graphics*, vol. 22, no. 3, pp. 477–484, 2003.

[24] M. A. Scott, *T-splines as a Design-Through-Analysis Technology*. PhD thesis, The University of Texas at Austin, 2011.

[25] M. A. Scott, X. Li, T. W. Sederberg, and T. J. R. Hughes, "Local refinement of analysis-suitable T-splines," *Computer Methods in Applied Mechanics and Engineering*, vol. 213, pp. 206–222, 2012.

[26] M. J. Borden, M. A. Scott, J. A. Evans, and T. J. R. Hughes, "Isogeometric finite element data structures based on Bézier extraction of NURBS," *International Journal for Numerical Methods in Engineering*, vol. 87, no. 1-5, pp. 15–47, 2011.

[27] M. A. Scott, M. J. Borden, C. V. Verhoosel, T. W. Sederberg, and T. J. R. Hughes, "Isogeometric finite element data structures based on Bézier extraction of T-splines," *International Journal for Numerical Methods in Engineering*, vol. 88, no. 2, pp. 126–156, 2011.

[28] L. Piegl and W. Tiller, "The NURBS book," *Monographs in Visual Communication*, 1997.

[29] D. F. Rogers, *An Introduction to NURBS with Historical Perspective*. Elsevier, 2000.

[30] M. Costabel, "Boundary integral operators on Lipschitz domains: elementary results," *SIAM Journal on Mathematical Analysis*, vol. 19, no. 3, pp. 613–626, 1988.

[31] G. Rodin and O. Steinbach, "Boundary element preconditioners for problems defined on slender domains," *SIAM Journal on Scientific Computing*, vol. 24, no. 4, pp. 1450–1464, 2003.

[32] T. J. R. Hughes, *The Finite Element Method: Linear Static and Dynamic Finite Element Analysis*. Dover Publications, 2000.

[33] B. Irons, O. C. Zienkiewicz, Y. K. Cheung, and G. P. Bazeley, "Triangular elements in plate bending conforming and nonconforming solutions," in *Conference of Matrix Methods, Wright-Patterson Air Force Base, Ohio*, 1965.

[34] W. G. Strang and G. J. Fix, *An analysis of the finite element method*. Prentice-Hall series in automatic computation, Prentice-Hall, 1973.

[35] R. L. Taylor, J. C. Simo, O. C. Zienkiewicz, and A. C. H. Chan, "The patch test - a condition for assessing FEM convergence," *International Journal for Numerical Methods in Engineering*, vol. 22, no. 1, pp. 39–62.

[36] C. Schwab and W. L. Wendland, "On numerical cubatures of singular surface integrals in boundary element methods," *Numerische Mathematik*, vol. 62, no. 1, pp. 343–369, 1992.

[37] J. D. Eshelby, "The determination of the elastic field of an ellipsoidal inclusion, and related problems," *Proceedings of the Royal Society of London A: Mathematical, Physical and Engineering Sciences*, vol. 241, no. 1226, pp. 376–396, 1957.

[38] D. Schillinger, L. Dede, M. A. Scott, J. A. Evans, M. J. Borden, E. Rank, and T. J. R. Hughes, "An isogeometric design-through-analysis methodology based on adaptive hierarchical refinement of NURBS, immersed boundary methods, and T-spline CAD surfaces," *Computer Methods in Applied Mechanics and Engineering*, vol. 249-252, pp. 116 – 150, 2012.

[39] S. G. Mogilevskaya and D. V. Nikolskiy, "The use of complex integral representations for analytical evaluation of three-dimensional BEM integrals - potential and elasticity problems," *Quarterly Journal of Mechanics and Applied Mathematics*, vol. 67, no. 3, pp. 505–523, 2014.

[40] V. Rokhlin, "Rapid solution of integral equations of classical potential theory," *Journal of Computational Physics*, vol. 60, no. 2, pp. 187–207, 1985.

[41] L. Greengard and V. Rokhlin, "A fast algorithm for particle simulations," *Journal of Computational Physics*, vol. 73, no. 2, pp. 325–348, 1987.

[42] N. Nishimura, "Fast multipole accelerated boundary integral equation methods," *Applied Mechanics Reviews*, vol. 55, no. 4, pp. 299–324, 2002.

[43] Y. Fu, K. J. Klimkowski, G. J. Rodin, E. Berger, J. C. Browne, J. K. Singer, R. A. Van De Geijn, and K. S. Vemaganti, "A fast solution method for three-dimensional many-particle problems of linear elasticity," *International Journal for Numerical Methods in Engineering*, vol. 42, no. 7, pp. 1215–1229, 1998.

[44] D. C. Thomas, L. Engvall, S. Schmidt, K. Tew, and M. A. Scott, "U-splines: splines over unstructured meshes." preprint, available from `https://coreform.com/usplines`, 2018.

A Representation of system matrices

In this appendix, we provide details helpful for formulating linear algebraic equations (9) and (10). The column-vectors are formed by grouping the Cartesian components into sub-column-vectors. Namely, the displacement column-vector has the structure

$$\underline{\tilde{u}} = \begin{pmatrix} \underline{\tilde{u}}_1 \\ \underline{\tilde{u}}_2 \\ \underline{\tilde{u}}_3 \end{pmatrix}.$$

Here $\underline{\tilde{u}}_1$ is the column-vector of length $n^{D,1}$. It contains the x_1 Cartesian components of the vector-valued coefficients approximating the field $\tilde{u}_1(x)$ with $x \in \Gamma_{N,1}$; see (8). The length of $\underline{\tilde{u}}$ is

$$n^D = n^{D,1} + n^{D,2} + n^{D,3}\,.$$

The structure of the column-vector $\underline{f}^S$ is exactly the same. The column-vectors $\underline{\tilde{t}}$ and $\underline{f}^H$ are structured similarly, but their blocks have length $n^{N,1}$, $n^{N,2}$, and $n^{N,3}$; the total length of each $\underline{\tilde{t}}$ and $\underline{f}^H$ is

$$n^N = n^{N,1} + n^{N,2} + n^{N,3}\,.$$

The column-vectors dictate the structure of the block-matrices representing the operators in (9) and (10). Accordingly, V is an $n^D \times n^N$ matrix, Σ^D and K are $n^D \times n^D$ matrices, I^N, Σ^N, and K' are $n^N \times n^N$ matrices, and D is an $n^N \times n^D$ matrix.

The components of the blocks of the system matrices are defined as

$$\begin{aligned}
\Sigma^D_{ij}[A,B] &= \sigma_{ij}(x^D_A) N^D_B(x^D_A), \\
\Sigma^N_{ij}[A,B] &= \sigma_{ij}(x^N_A) N^N_B(x^D_A), \\
I^N_{ii}[A,B] &= N^N_B(x^D_A),
\end{aligned}$$

and

$$\begin{aligned}
V_{ij}[A,B] &= \mathcal{V}_{ij} N^N_B(x^D_A) \\
&= \int_\Gamma U_{ij}(x^D_A, y) N^N_B(y) ds_y, \\
K_{ij}[A,B] &= \mathcal{K}_{ij} N^D_B(x^D_A) \\
&= \int_\Gamma \gamma_{ik} \left[U_{kj}(x^D_A, y), y \right] N^D_B(y) ds_y, \\
K'_{ij}[A,B] &= \mathcal{K}'_{ij} N^N_B(x^N_A) \\
&= \int_\Gamma \gamma_{ik} \left[U_{kj}(x^N_A, y), x^N_A \right] N^N_B(y) ds_y, \\
D_{ij}[A,B] &= \mathcal{D}_{ij} N^D_B(x^N_A) \\
&= -\int_\Gamma \gamma_{ik} \left\{ \gamma_{kl} \left[U_{lj}(x^N_A, y), y \right], x^N_A \right\} N^D_B(y) ds_y.
\end{aligned}$$

In these definitions, no summation is implied over repeated indices i and j. The components of the blocks of the right-hand-side vectors are

$$\begin{aligned}
\underline{f}_i^S[A] &:= f_i^S(x_A^D) \\
&= \sigma_{ij}(x_A^D)\tilde{g}_j(x_A^D) + \mathcal{K}_{ij}\tilde{g}_j(x_A^D) - \mathcal{V}_{ij}\tilde{h}_j(x_A^D), \\
\underline{f}_i^H[A] &:= f_i^H(x_A^N) \\
&= \mathcal{D}_{ij}\tilde{g}_j(x_A^N) - \left[\delta_{ij} - \sigma_{ij}(x_A^N)\right]\tilde{h}_j(x_A^N) + \mathcal{K}'_{ij}\tilde{h}_j(x_A^N).
\end{aligned}$$

Here no summation is implied over repeated indices i.

B Details of numerical integration

In this paper we extended the integration scheme adopted in [10] by introducing two hierarchical partitioning schemes, one for elements with large curvatures and aspect ratios, and the other for more efficient near-singular integration. In both schemes, decisions must be made on partitioning a given Bézier element (or sub-element) $\varphi(e)$. Those decisions require one to compute distances, curvatures, and aspect ratios. Once the new hierarchical partitioning schemes have been implemented, the numerical integration schemes adopted in [10] are applied to the generated integration mesh rather than the original Bézier mesh. In the remainder of this appendix, we provide details of criteria used for generating the integration mesh.

To eliminate elements with large curvatures we adopt the following scheme:

1. For a given $\varphi(e)$, compute the tangential gradient of the unit normal field to $\varphi(e)$ and thus form a 3×2 matrix.

2. Compute the maximum principal value Λ of the 3×2 matrix.

3. Use the 5×5 Gaussian integration rule to compute $\kappa := \|\Lambda\|_{L^{10}}$ as an approximation of $\|\Lambda\|_{L^\infty}$.

4. Use the 4×4 Gaussian integration rule to compute the area A of $\varphi(e)$; define the element size $h := \sqrt{A}$.

5. Identify a quadrilateral by connecting the vertices of $\varphi(e)$ by straight segments. Denote the lengths of those segments by l_1 through l_4, so that l_1 (l_2) and l_3 (l_4) are opposite of each other. Define the aspect ratio of $\varphi(e)$ as

$$\chi = \max\left(\frac{l_1 + l_3}{l_2 + l_4}, \frac{l_2 + l_4}{l_1 + l_3}\right).$$

6. If $\kappa h > 1/8$ and $\chi > 3$ then partition e into two subdomains, so that the aspect ratio of each subdomain is less than χ. If $\kappa h > 1/8$ and $\chi < 3$ then partition e uniformly into four subdomains. If $\kappa h \leq 1/8$ then no partitioning is necessary.

7. Repeat the steps until $\kappa h \leq 1/8$ on each subdomain.

This scheme is valid for elements that do not involve collapsed edges. If $\varphi(e)$ contains a collapsed edge, and $\kappa h > 1/8$, then $\varphi(e)$ is partitioned into a triangle and trapezoid as shown in Figure 20.

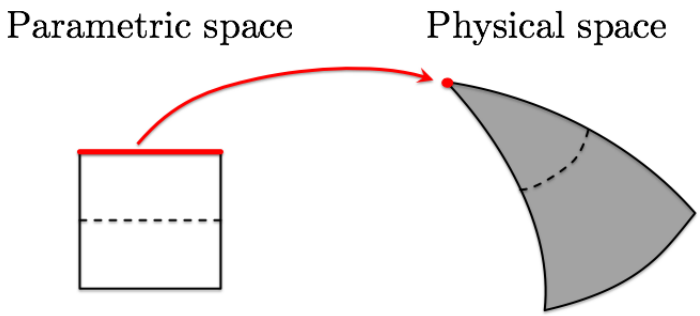

Figure 20: Partitioning of an element containing a collapsed edge. The collapsed edge is shown in red. The dashed line bisects the square.

Once the curvature has been reduced for all elements and sub-elements, elements and sub-elements with large aspect ratios are eliminated by bisecting domains until $\chi \leq 3$ for each subdomain.

In the near-singular integration scheme in [10], $\varphi(e)$ is partitioned when

$$d \leq 3h \,,$$

where d is the physical distance between a collocation point P, at which the integral is evaluated, and $\varphi(e)$. Here we retain this criterion, but replace the algorithm for computing the distance with a more efficient one:

1. Assign node numbers to $\varphi(e)$ (Fig. 21).
2. Approximate $\varphi(e)$ by two flat triangles whose vertices are the nodes 1, 2, and 3, and 3, 4, 1. (Fig. 21).
3. Compute the distances between P and each of the triangles, and define the first approximation d_1 as the minimum of the two.

4. Partition $\varphi(e)$ into four quadrilaterals, and then each quadrilateral into two flat triangles.

5. Compute the distances between P and each of the four quadrilateral subdomains following the previous steps; define the second approximation d_2 as the minimum among the four distances.

6. If
$$|d_1 - d_2| < \frac{1}{2}|d_2 - 3h| \,,$$
then accept d_2 as an estimate of the distance. Otherwise, further partition the four quadrilaterals, and compute the third approximation d_3. If
$$|d_2 - d_3| < \frac{1}{2}|d_3 - 3h| \,,$$
then accept d_3 as an estimate of the distance. Otherwise continue the partitioning scheme until a sufficient approximation of d is obtained.

If $\varphi(e)$ contains a collapsed edge, then an approximation to the distance can be computed using one rather than two triangles.

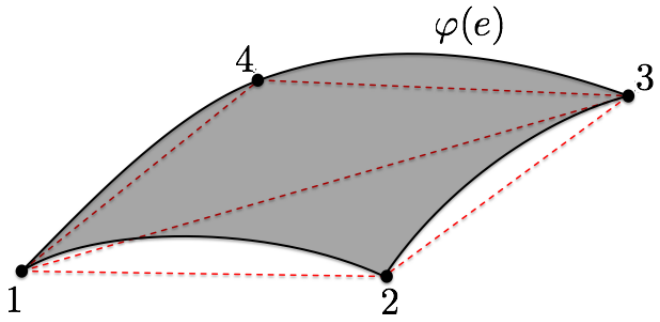

Figure 21: Approximation of $\varphi(e)$ by two interpolating triangles. The numbers denote the numbers assigned to each node of $\varphi(e)$; the interpolating triangles are shown in dashed red lines.

The proposed scheme for estimating d is by far more efficient than the one based on constructing a bounding ball for $\varphi(e)$ and adopted in [10]. However, unlike the old scheme, the proposed scheme is not robust. Nevertheless, our numerical experiments suggest that the proposed scheme yields essentially the same accuracy.

C Regularization of operators

Similar to BIEs corresponding to Laplace's equation, the SBIE and the HSBIE corresponding to the equations of linear elasticity involve weakly-singular, singular and hyper-singular integrals. In this section we establish that the evaluation of all integral operators at a point $x \in \Gamma$ can be reduced to the evaluation of weakly-singular integrals.

The single-layer operator is naturally weakly singular; while the same is true for the double-layer operators associated with Laplace's equations, this is not true for the double-layer operators associated with Navier's equations. Nevertheless, it can be easily seen that

$$\sigma_{ij} + \mathcal{K}_{ij} 1 = 0, \quad \text{for all } i, j = 1, 2, 3$$

and therefore

$$\left(\sigma_{ij} + \mathcal{K}_{ij}\right) u_j(x) = \int_\Gamma \gamma_{ik}\left[U_{kj}(y, x), y\right] \left[u_j(y) - u_j(x)\right] ds_y$$

for all $i, j = 1, 2, 3$. If u_j is Lipschitz continuous, so that

$$|u_j(y) - u_j(x)| < C|y - x|,$$

then the integral becomes weakly singular. This additional restriction on $u_j(x)$ is automatically satisfied for each basis function, and therefore the double layer operator can be evaluated as a weakly-singular integral.

To regularize the adjoint double-layer operator, first, one can establish that for any x and y on the smooth part of Γ

$$\left|\gamma_{ik}\left[U_{kj}(y, x), y\right] - \gamma_{ik}\left[U_{kj}(x, y), x\right]\right| \leq \frac{C}{|x - y|}. \tag{15}$$

Then the adjoint double-layer operator can be expressed as

$$\begin{aligned}
&\left[(\delta_{ij} - \sigma_{ij}) - \mathcal{K}'_{ij}\right] t_j(x) = \\
&\quad t_i(x) - \left(\sigma_{ij} + \mathcal{K}_{ij}\right) t_j(x) - \int_\Gamma \left\{\gamma_{ik}\left[U_{kj}(x, y), x\right] - \gamma_{ik}\left[U_{kj}(y, x), y\right]\right\} t_j(y) ds_y \\
&\quad .
\end{aligned}$$

Following the proof for the double-layer operator, the second term on the right-hand side is weakly-singular as long as t_j is Lipschitz continuous in the vicinity of x. This condition holds for x on the smooth part of Γ. The last term on the right-hand side is weakly-singular because of (15).

The hyper-singular operator is regularized using exactly the same technique as for Laplace's equation [10].